CHAPTER IV

HIGH PERFORMANCE AND STABILITY OF COPPER LOADING ON MESOPOROUS CERIA CATALYST FOR THE PREFERENTIAL OXIDATION OF CO

4.1 Abstract

Copper (Cu) supported on mesoporous (MSP) ceria catalysts with different Cu loadings were prepared by deposition-precipitation (DP) method for the preferential CO oxidation in a H_2-rich stream (CO-PROX). The synthesized MSP ceria with high surface area of 293.2 m^2/g and ordered structure provides higher capacity to release the lattice oxygen to theoretically oxidize CO than commercial ceria. All copper-MSP ceria catalysts show high dispersion of Cu and still maintain fluorite structure of MSP ceria. Moreover, TEM image also showed the three dimensional and long-range order of pore structure of Cu-catalysts. The reduction temperature of the Cu-catalysts shift to the lower temperature comparing to pure MSP ceria and the reduction of Ce^{4+} to Ce^{3+} is decreasing when increasing the copper content. The MSP ceria catalyst with 7 wt% Cu loading (7Cu/MSP ceria) shows the highest activity at 110 °C with 100 % CO conversion, and the temperature at 100 % CO conversion shifts to 130 °C in the presence of CO_2 and H_2O. Moreover, the 7Cu/MSP ceria also performs the high stability over 48 h in various feed components, making attractive for using as a catalyst in purification of hydrogen. The high stability of 7Cu/MSP ceria was confirmed by various techniques which show a slight change of the fluorite structure and surface composition.

Keywords: Mesoporous Ceria; High Surface Area; CO-PROX; Copper Catalyst; Deposition-precipitation

4.2 Introduction

Hydrogen (H_2) is very attractive for using in proton exchange membrane (PEM) fuel cell due to readily available gas, renewable energy source, no hazard, friendly environment, and fuel efficacy. However, the major problem in the PEM fuel cells is the need of high-purity of H_2 [1]. The preferential CO oxidation (PROX) reaction has been widely used in the purification process of H_2 due to its low cost and ability to reduce CO content to less than 10 ppm without excess hydrogen consumption.

Ceria has been widely investigated in the automotive exhaust purification, oxygen storage, and catalysis via conversion between Ce^{3+} and Ce^{4+} oxidation states, oxygen storage and release properties [2-4]. The catalytic performance of ceria can be increased by its structural properties, such as surface area and crystal morphology [5,6].

Mesoporous (MSP) materials provide superior performances in allowing a large reactant to penetrate inside the pores due to their pore size between 2–50 nm and high surface areas. Thus, they have attracted particular attention in many applications, as adsorption, catalysis, sensor, and hosts for the synthesis of nanomaterials [7]. The first group of MSP materials discovered by Mobil group (M41S family) consists of hexagonal MCM-41, cubic MCM-48, and unstable lamellar MCM-50 mesostructures [8]. Cubic MCM-48 indexed in the space group of *Ia3d* is the most attractive material in terms of catalytic activity due to its three-dimensional pore structure and interconnected channels, reducing the diffusion limitations and avoiding the pore blocking of coming molecule [9].

Deeprasertkul *et al.* [10] synthesized MSP ceria via nanocasting method using high surface area MCM-48 as a template. The synthesized MSP ceria has high surface areas with strong reduction at lower temperature than commercial ceria. However, the pure MSP CeO_2 still has too high reduction temperature to be used as a catalyst in the PROX reaction. It was reported that the structural modification of CeO_2 lattice by doping with transition metal oxides may improve its stability and activity [11].For example, loading copper (Cu) to commercial CeO_2 exhibited a higher activity and selectivity in CO oxidation [12-15]. The Cu-loading on a support

was prepared by the deposition-precipitation (DP) method which has an advantage over other methods in terms of uniform particle distribution with small particle size [16] and a closed interaction between the metal particles and the support [17].

In this work, Cu loaded onto MSP ceria with different percentages of Cu loading by the deposition-precipitation (DP) method was prepared and characterized, followed by determining the catalytic activity and stability for the PROX reaction using various feed components. All prepared copper catalysts were characterized by various techniques to study the relationship between the properties and the performance.

4.3 Experimental

4.3.1 Materials

Fumed silica (SiO_2, 99.8%, Nippon Aerosil, Japan), HP grade nitrogen (N_2, 99.98% purity, Thai Industrial Gases Public Company Limited (TIG), Thailand), ethylene glycol (EG, 99%, J.T. Baker, USA), triethanolamine (TEA, QRëc chemical, Thailand), acetonitrile (CH_3CN, 99.9%, Labscan, Thailand), cerium(III)nitrate hexahydrate ($Ce(NO_3)_3.6H_2O$, 99%, Sigma-Aldrich, Germany), ethanol (CH3CH2OH, 99.9%, Labscan, Thailand), sodium hydroxide (NaOH, 99%, Labscan, Thailand), cetryltrimethylammonium bromide (CTEB, 96.0%, Fluka, Germany), copper(II)nitrate trihydrate ($Cu(NO_3)_2.3H_2O$, 99.5%, Merck, Germany), hydrogen tetrachloroaurate(III) trihydrate ($HAuCl_4.3H_2O$, 49.0% Au basis, Sigma-Aldrich, Germany), and sodium carbonate (Na_2CO_3, 99.8%, Ajax, Thailand) were used without further purification.

4.3.2 Catalyst Preparation

Following Deeprasertkul's synthetic method [10], the MSP ceria was prepared via nano casting method by mixing 50 wt% of cerium nitrate as a precursor with MCM-48 as a template in 5 ml of ethanol. After 30 min stirring, the ethanol in the mixture was removed by evaporation in an oven at 100 °C. The dried powder was calcined in air at 550 °C for 6 h to decompose the nitrate species. After that, the solid

was removed the silica template by using 2 M NaOH at 50 °C for 3 times and washed with deionized water until neutral and finally dried over night at 80 °C.

CuO/MSP ceria catalysts were prepared by deposition-precipitation (DP) from aqueous solution of $Cu(NO_3)_2.3H_2O$ with different loadings of Cu (3, 5, 7 and 9 wt%). The mixture was stirred at room temperature for 1 h, heated to 80 °C, and adjusted its pH to 7. The mixture was then aged for 1 h to obtain crude solid product. The solid was filtered, washed with warm distilled water, dried over night at 80 °C, and finally calcined in air at 500 °C for 6 h.

4.3.3 Catalyst Characterization

The silica residual was determined by X-ray fluorescence spectrophotometer (XRF) technique on PANalytical AXIOS PW 4400 and the actual content of copper loaded on MSP ceria was determined by atomic adsorption spectroscopy (VARIAN Model 300/400). Mesoporous phase and crystallinity of the prepared catalysts were evaluated by Small Angle X-Ray Diffraction (SAXD) (Rigaku TTRAX III) with a scanning speed of 1 $^{o}min^{-1}$ and CuKα source (λ= 0.154 Å) in a range of 2θ = 2–6°. Wide Angle X-Ray Diffraction (WAXD) was performed on a Rigaku Smartlab® with a scanning speed of 1 ^{o} and 0.1 $^{o}min^{-1}$ and CuKα source (λ= 0.154 Å) in a range of 2θ = 20–80° to investigate the metal nano-crystals and dispersions. Crystallite sizes of ceria and CuO were determined by using Scherrer equation with Scherrer constant of 0.94 for spherical cubic crystals [18]. Moreover, the lattice parameter (a) was estimated as the cubic phase. The specific surface area and pore size distribution of the catalysts were determined by N_2 adsorption-desorption isotherms (Quantachrome Autosorb-1). Transmission electron microscopy (TEM) images were characterized on a JEOL JEM-2100F TEM instrument. The samples were prepared by dispersing in methanol and then the solution was dropped on a holly carbon grid and dried at room temperature. The photographs were taken at an accelerating voltage of 200 kV. Diffuse reflectance Ultraviolet-visible (UV-vis) spectra (DRS) were recorded in a range of 200–900 nm on a Shimadzu UV-2500 using $BaSO_4$ as a reference. The reflectance spectra were converted by the Kubelka-Munk function into an absorption spectra [19] and fitting

with polynomial function. X-ray photoelectron spectroscopy (XPS) was used to characterize the surface composition and oxidation state of the surface elements measured on Kratos AXIS Ultra DLD spectrometer with a monochromatic Al-Kα X-ray source (15 kV). The pressure in the analysis chamber was lower than 5 x 10^{-7} Torr. The survey spectra were observed in the binding energy (BE) between 0 to 1200 eV. The detail spectra were obtained for the C 1s, O 1s, Ce 3d and Cu 2p regions. The charging effect was subtracted by fixing C 1s peak at the binding energy of 284.9 eV. Raman spectra were carried out using a Senterra dispersive Raman microscope (Btuker Optics) with 532 nm ion-argon laser, 20 mW power laser. For each sample, the spectral range was observed between 4500–70 cm^{-1}.

The redox properties were evaluated by temperature-programmed reduction under hydrogen (H_2-TPR) using 50 mg sample. The samples were pretreated in N_2 at 250 °C for 30 min, and then cooled to room temperature. H_2-TPR profiles were observed from room temperature to 900 °C with a heating rate of 10 °C min^{-1} in 5.13 % H_2/N_2 (20 ml min^{-1}). Hydrogen consumption was detected by a thermal conductivity detector (TCD).

4.3.4 Activity Measurement

All catalytic activity measurements for PROX were evaluated in a fixed-bed U-tube micro-reactor at atmospheric pressure by packing 100 mg of the 80–120 mesh catalyst. The activity was investigated at various temperatures (50–250 °C). The composition of feed gas (in %vol) for PROX reaction was $H_2/O_2/CO$ = 40/1/1, balanced in He with a total flow rate of 50 ml min^{-1}. The influent and effluent gases were analyzed by auto-sampling equipped in an on-line gas chromatograph (Agilent Technologies 6890N) equipped with a packed carbosphere column (80/100 mesh and 10 ft x 1/8 inch) and a thermal conductivity detector (TCD). The CO conversion or catalytic activity calculations were based on the CO consumption and the CO selectivity determined by the ratio of O_2 consumption for CO conversion reaction to the total O_2 consumption. Moreover, The effect of the feed component on the catalyst performance for the PROX reaction was studied by adding 10 vol% CO_2 and 10 vol% water into influent gases with maintaining a composition of H_2/O_2,/CO at 40/1/1 with a total flow rate of 50 ml min^{-1}.

4.4 Results and Discussion

4.4.1 Characterization of Pure MSP Ceria

The ordered MSP ceria synthesized from MCM-48 template via nanocasting, the negative replica of the MCM-48 template, shows the same characteristic diffraction peaks, see SAXD pattern in Fig. 4.1-inset at {211} and {220}, consistent with the work reported by Longloilert et al. work [10]. This result confirms that the MSP ceria still retains some order from the MCM-48 template. Moreover, the crystallinity of the MSP ceria also confirmed by WAXD in Figure 4.1, showing peaks at 2θ = 29°, 33.2°, 47.2°, 55.3°, 59.1°, 69.3°, 76.8°, and 78.9°, corresponding to the peaks of the cubic fluorite structured ceria [20,21]. The absence of the peak at 2θ = 22°, belonging to the peak of amorphous silica, refers to no silica template in the final product. Moreover, the silica template residual determined by XRF technique indicated a small amount of silica remaining (8 %wt) in the ordered MSP ceria after removal of the template. The N_2 adsorption-desorption isotherm in Fig. 2 showed a type IV isotherm with H3 hysteresis loop, relating to MSP materials with slit-like pores [22]. The pore size distribution curve (inset) in Figure 4.2 presented the sharp peak with the average pore diameter of 5.79 nm, confirming the uniform pores in the prepared MSP ceria. Moreover, its BET specific surface area was observed 293.2 m^2/g which is higher than commercial ceria (Rhodia, S_{BET} = 164 m^2/g, average pore diameter = 4.0 nm).

4.4.2 Characterization of Cu Loaded on MSP Ceria

Physical properties of the synthesized catalysts are shown in Table 4.1. The percentage of Cu loading determined by AAS measurement is very close to the theoretical value, indicating that the deposition-precipitation is a very suitable and effective method for depositing Cu onto MSP ceria [23]. It is not surprising that addition of Cu decreased the BET surface area of the material, as compared to the pure ceria, especially 9 wt% Cu loading dramatically decreased about 31 % surface area.

The WAXD patterns of all prepared catalysts in Figure 4.3 show the main diffraction peaks at 2θ = 29°, 33.2°, 47.2°, 55.3°, 59.1°, 69.3°, 76.8°, and 78.9°,

corresponding to the fluorite-type cubic crystal structure of the ceria phase [20,21]. Interestingly, there are no diffraction peaks of CuO phases in all copper loading catalysts at $2\theta = 35.6°$ and 38.8°, probably due to either the high dispersion of the Cu or the low detection limit at these copper concentrations. To confirm whether the CuO was well- dispersed, all Cu loading catalysts were submitted for a longer scan time, as illustrated in (inset) Figure 4.3, and the results still showed the absence of the Cu diffraction peaks, suggesting that the DP method provides the high dispersion of Cu on MSP ceria. One of the reasons was probably from the strong interaction between copper and ceria, as reported by Liao *et al.* [23]. The average size of ceria crystallites for all catalysts (Table 4.1), calculated from the diffraction peak broadening at $2\theta = 29°$ using Scherrer's equation, are not different from that of the pure MSP ceria. The average crystallite size of MSP ceria obtained was very small, comparing to commercial ceria (larger than 5.0 nm) [24,25], resulting from a large number of oxygen vacancies in the fluorite structure crystallites [26,27]. The catalytic activity of ceria is proportional to the number of oxygen vacancies in the crystal [28]. The lattice parameter (a) of all prepared catalysts, calculated from the main diffraction peaks of ceria cubic phase, showed similar values to the pure MSP ceria. Moreover, the variation in the cell parameters after introducing Cu onto ceria lattice, as illustrated in Figure 4.4, showed slightly different. As a result, it could be concluded that the Cu loaded on MSP ceria still retained the fluorite structure.

To confirm whether Cu species were highly dispersed in the MSP ceria and still retained the MSP structure, as indicated by the XRD results, TEM was carried out. However, because of the low contrast between Cu and ceria, it was not possible to see the dispersion of CuO [29], as shown in Figure 4.5. This figure illustrates that the morphology of 7Cu/MSP ceria still retains the long-range order in the pore arrangement among the nanoparticles and three-dimensional pore structure. The average size of ceria crystallites was similar to that obtained from the x-ray line, which was about 3.5 nm.

Some studies reported that XPS technique was able to characterize the surface composition of ceria-based catalysts [30-33]. Thus, in this study, the average percent weight of surface compositions was determined and shown in Table 4.2 Each

Cu containing catalyst was detected for 5 points. Interestingly, all catalysts showed much lower Cu percentages at the surface than those obtained by AAS analysis from the bulk. As discussed previously, the XRD results showed the high dispersion with no accumulated copper. It can be rationalized that most of copper species were embedded inside the pore of MSP ceria since the average pore diameter of MSP ceria (5.79 nm) that is larger than Cu species (0.07 nm). Moreover, the elemental oxidation states of both fresh and used catalysts from the stability tests (denoted as –P3, P2, and P1 for the systems containing both CO_2 and water, only CO_2, and no CO_2 and water, respectively.) were analyzed by XPS.

The O 1s spectra of all catalysts are presented in Figure 4.6 The surface oxygen consists of 2 peaks, corresponding to 2 species. The first peak at binding energy (BE) of about 530–533 eV is assigned to the adsorbed oxygen or the oxygen in the hydroxy-like groups [34], while the second peak at BE around 527–529 eV belongs to the lattice oxygen in ceria and CuO. The amount of lattice oxygen seems to be proportional to the percent of Cu loading and all fresh catalysts present the higher amount of lattice oxygen than the used catalysts, as shown in Table 4.2

The Ce 3d region spectra were deconvoluted to eight peaks, as can be seen in Figure 4.7 The Ce 3d core level spectra corresponding to Ce^{4+} oxidation state are composed of six contributions, viz. v, u, v', u', v'', and u'', and the four peaks consisting of v^o, u^o, v', and u' correspond to Ce^{3+} ions. The amount of Ce^{3+} on the surfaces of ceria based catalysts can be estimated using the following equation [35].

$$Ce^{3+}(\%) = \frac{S(Ce^{3+})}{S(Ce^{3+} + Ce^{4+})} \times 100 \qquad (1)$$

All fresh and used catalysts show high amounts of Ce^{3+} around 37–40 % which might be due to either the photo-reduction of ceria in the analysis chamber or the thermal treatment during the preparation [36], as shown in Table 4.2 The amount of Ce^{3+} after gone through the PROX reaction ($7CuO/CeO_2$-P1, $7CuO/CeO_2$-P2 and $7CuO/CeO_2$-P3) is slightly decreased from the corresponding fresh catalyst, resulting from the reduction of Ce^{3+} to Ce^{4+}.

In Figure 4.8, the Cu 2p core level spectra for all samples present three main peaks of $Cu2p_{3/2}$, shake-up, and Cu $2p_{1/2}$ at around 933, 939–947, and 953 eV, respectively. The shake-up satellite peak indicates the existence of the Cu^{2+} oxidation state while the Cu $2p_{3/2}$ peak represents both Cu^{+} and Cu^{2+} species which are generally difficult to distinguish [37]. The decreasing of the ratio between the intensities of the shake-up satellite and the Cu $2p_{3/2}$ peaks ($I_{Cu,sat}/I_{Cu,2p3/2}$) and the shift of satellite peak toward the lower BE are corresponding to the reduction of Cu^{2+} to a lower oxidation or metallic state [23]. However, the ratio of $I_{Cu,sat}/I_{Cu,2p3/2}$ and the satellite peak position of the used catalysts are slightly different from the fresh catalysts, as shown in Table 4.2 Not only a little change in Cu 2p core level spectra but also a slight difference in Ce 3d region of the used and the fresh catalysts could be indicated that the reaction took place inside the pore of MSP ceria, resulting in a slight change in the metal species at the surface.

The surface structure of the Cu loading catalysts was characterized by DR UV-Vis and the data were fitted with polynomial function with order 3, as shown in Figure 4.9 Pure ceria presents the strong absorption band at λ less than 400 nm, corresponding to a band gab around 3.1 eV, with the other band in the range of 300–375 nm, attributing to localized O-Ce charge transfer transitions involving a surface Ce^{4+} ions [38,39]. Pure CuO, obtained by calcination of $Cu(NO_3)_2.3H_2O$ at 500 °C for 6 h, shows the absorption band at λ = 360.0 nm, corresponding to charge transfer between O^{2-} and Cu^{2+} [40], and the intensity of this absorption band relates to the amount of CuO on the surface [41]. All Cu loading samples show that the absorption band is shifted to the lower wavelength, indicating to the highly dispersed CuO, in agreement with the XRD results. However, the intensity of this absorption band does not increase with percent of Cu, implying that there is a slight difference of Cu content on the surface, consistent to the XPS results described above.

4.4.3 Reduction Property of Cu Loaded on MSP Ceria

According to studies cited elsewhere [42,43] , the H_2-TPR profile in Figure 4.10 (inset) presents two reduction peaks at 320°–650 °C and 680°–880 °C, corresponding to the reduction of the surface-capping oxygen and the bulk-phase

lattice oxygen [42,43], respectively. The highest intensity of the former peak was observed on the ordered MSP ceria relating to the high surface area [10]. It is worth noting that the pure CuO has only one TPR peak at 380°–392 °C [44]. In this study, the reduction profiles of all Cu/MSP ceria were shifted to the lower temperature at 180° and 230 °C. The low temperature peak is related to highly disperse Cu species on the surface not directly interacting with the support. The second peak at the higher temperature is related to the bulk CuO, simultaneous reductions of surface layers of CeO_2 and highly disperse CuO in direct contact with ceria [45,46]. The theoretical and experimental hydrogen (H_2) consumptions for all samples are shown in Table 4.3 The spill-over of H_2 consumption of the second peak to the theoretical H_2 required for a complete reduction of CuO ($CuO + H_2 \rightarrow Cu + H_2O$) relates to the H_2 consumption for the reduction of Ce^{4+} to Ce^{3+} [47]. Thus, the reduction of Ce^{4+} to Ce^{3+} decreases with increasing the Cu content.

4.4.4 Catalytic Performance for PROX

4.4.4.1 Effect of Feed Components

Catalytic performances of all Cu loading catalysts were evaluated for PROX reaction under an excess H_2 component in the temperature range of 50°–250 °C, see Fig 4.11 a-b. All Cu/MSP ceria showed the higher activity than the pure ceria which has T_{50} at 310 °C. The catalysts with 7 and 9% Cu loadings achieve 100% conversion at 110 °C while the others reached 100% conversion at 130 °C. At low temperature, the catalytic activity is proportional to the amount of the lattice oxygen at the surface (see table 4.2) which can provide oxygen to CO molecule easily [48], resulting in the higher activity. Moreover, all catalysts provided the CO conversion greater than 90 % at the temperature below 170 °C. The oxygen selectivity towards CO_2 decreases with temperature, especially, 9% Cu/MSP ceria showed a dramatic decrease of selectivity. At the temperature below 110 °C, all catalysts, except $9Cu/CeO_2$, have the selectivity above 80 %. As previously indicated, $3Cu/CeO_2$, $5Cu/CeO_2$ and $7Cu/CeO_2$, providing higher activity and selectivity, were thus chosen to further study the effect of CO_2 in the PROX reaction. It was found that the activity and selectivity of all studied catalysts were shifted to

the higher temperature in the presence of CO_2, as shown in Figure 4.11c-d. The decrease in the catalytic performance might be due to the competitive adsorption of CO and CO_2 [37] and the formation of carbonates on interfacial ceria sites, resulting in diminishing CuO-CeO_2 interfacial redox activity [49]. All catalysts showed the 100 % conversion at 130 °C with different reaction rates. The 7Cu/CeO_2 has the highest rate at the temperature below the maximum % conversion temperature. The selectivities of all catalysts were slightly different at the temperature below 170 °C. Moreover, the 7Cu/CeO_2 showed the lowest H_2 consumption (not shown) of 1% at 130 °C while 3Cu/CeO_2 and 5Cu/CeO_2 consumed about 7 %. Therefore, 7Cu/CeO_2 was used to study the effect of both 10% CO_2 and H_2O in the PROX reaction, as resulted in Figure 4.11e. The activity was extremely shifted to the higher temperature, as compared to the feed free of both gases. Moreover, the position of 100% CO conversion was also shifted to 150 °C. This phenomenon can be explained by the competitive adsorption of CO and CO_2 and the blocking effect of water [37].

4.4.4.2 Stability of 7Cu/CeO_2 Catalyst

From previous results, 7Cu/CeO_2 shows the best performance in the PROX reaction at various feed streams. The time-on-stream performance of 7Cu/CeO_2 catalyst in a feed free of CO_2 and water, the presence of CO_2 was collected at 130 °C while in the presence of CO_2 and H_2O the catalyst was performed at 150 °C. The CO conversion of 7Cu/CeO_2 catalyst was maintained at 100 % for a period of 48 h in all feed streams (not shown), showing an impressive performance and stability of the catalyst. Moreover, the catalyst was also confirmed its stability using XPS analysis which showed slightly different surface composition of 7Cu/CeO_2 before and after the PROX reaction. Moreover, the structure of catalyst after the stability test was characterized by Raman spectrometer to observe the vibrational modes corresponding to the arrangement of atom [50], and the results (not shown) showed that the fresh 7Cu/CeO_2 consists of four peaks at 109.57, 451.50, 585.36, and 1107.40 cm^{-1}. The main peak of the catalyst appeared at wavenumber around 451–447 cm^{-1}, as shown in Figure 4.12, which is related to a triple degenerated F_{2g} mode [51]. The used catalyst showed the systematic shift of the F_{2g} mode to the lower frequencies due to the lattice expansion, resulting from the

occurrence of oxygen vacancies while two Ce^{3+} ions (ionic radius 1.143 Å) replace two Ce^{4+} ions in the oxidation of CO [52-54]. The increasing of Ce^{3+} after the PROX reaction was also confirmed by XPS analysis, as summarized in Table 4.2. Especially, the used catalyst in the presence of 10 % CO_2 and 10 % H_2O showed the largest change in Raman shift, indicating more generated vacancies due to the occurrence of water-gas shift reaction. This reaction becomes more important at higher temperatures and more water vapor, resulting in increasing a lot of oxygen vacancies. The distortion of the fluorite structure can be confirmed by XRD shown in Figure 4.13. The average cell parameter of the cubic crystal structure was slightly changed, but the variation in the cell parameters calculated from each plane was larger, as compared to the fresh catalyst. However, the lattice parameter and the F_{2g} mode between the fresh and the used catalysts are slightly different. It can be concluded that the synthesized Cu/MSP ceria is highly stable and effective since it still maintains the structure during the PROX reaction.

4.5 Conclusions

The MSP ceria synthesized by nanocasting shows high order structure, high surface area of 293.2 m^2/g, and small crystallite size, giving a lot of oxygen vacancies in the crystal. All Cu loaded onto catalysts present high dispersion of Cu, as confirmed by DRUV, with slightly different physical properties, still maintaining the fluorite structure of MSP ceria. Moreover, the TEM image also confirms the three-dimensional and long-range order of pore structure. XPS analysis indicates the lower Cu contents from the surface than that from the bulk value analyzed by AAS analysis, referring to the penetration of copper precursor into the pore of MSP ceria. The reduction temperature of Cu catalysts was shifted to the lower temperature than that of the pure MSP ceria. Moreover, the reduction of Ce^{4+} to Ce^{3+} is inversely proportion to the copper content.

Among all synthesized Cu/MSP ceria, $7Cu/CeO_2$ presents 100% conversion at 110 °C and 87% selectivity toward CO_2 in an excess H_2 and a feed free of CO_2 and H_2O. In the presence of 10 % CO_2 or 10 % CO_2 with 10 % H_2O, the catalytic activity of $7Cu/CeO_2$ provides 100% CO conversion at higher temperatures (130° and 150

°C, respectively) due to the competitive adsorption of CO and CO_2, and the blocking effect of H_2O. Moreover, $7Cu/CeO_2$ is a highly stable catalyst over 48 h in a feed free of CO_2 and H_2O, the presence of CO_2, or the presence of CO_2 and H_2O, as confirmed by XRD, Raman spectrometer, and XPS analysis.

4.6 Acknowledgements

This research is financially supported by The Ratchadapisake Sompote Endowment Fund, and The Center of Excellence for Petrochemical and Materials Technology, Chulalongkorn University, Thailand.

4.7 References

1. D. Candusso, F. Harel, A.D. Bernardinis, X. Francois, M.C. Pera, D. Hissel, P. Schott, G. Coquery, International Journal of Hydrogen Energy 31 (2006) 1019.
2. T. Bunluesin, R.J. Gorte, G.W. Graham, Applied Catalysis B 15 (1998) 107.
3. T. Bunluesin, H. Cordatos, R.J. Gorte, Journal of Catalysis 157 (1995) 222.
4. X. Wang, R.J. Gorte, J.P. Wagner, Journal of Catalysis 212 (2002) 225.
5. C.T. Kresge, M. E. Leonowica, W.J. Roth, J.C. Vartuli, Nature 359 (1992) 710.
6. J.S. Beck, J.C. Vartuli, W.J. Roth, M.E. Leonowica, C.T. Kresge, K.D. Schmitt, C.T.W. Chu, D.H. Olson, Journal of the American Chemical Society 114 (1992) 10834.
7. V. Idakiev, T. Tabakova, A. Naydenov, Z.Y. Yuan, B.L. Su, Applied Catalysis B 63 (2006) 178.
8. C.T. Kresge, M.E. Leonowicz, W.J. Roth, J.C. Vartuli, J.S. Beck, Letters to nature 359 (1992) 710.
9. A. Monnier, F. Schuth, Q. Huo, D. Kumar, D. Margolese, R.S. Maxwell, M. Stucky, G.D. Krishnamurty, P. Petroff, A. Firouzi, M. Janicke, Science 261 (1993) 1299.

10. C. Deeprasertkul, R. Longloilert, T. Chaisuwan, S. Wongkasemjit, Materials Letters 130 (2014) 218.
11. A. Trovarelli, C.D. Leitenburg, M. Boaro, G. Dolcetti, Catalysis Today 50 (1999) 353.
12. G. Jacobs, S. Khalid, P.M. Patterson, D.E. Sparks, B.H. Davis, Applied Catalysis A 268 (2004) 255.
13. N.K. Gamboa-Rosales, J.L. Ayastuy, M.P. Gonzalez-Marcos, M.A. Gutierrez-Ortiz, Catalysis Today 176 (2011) 63.
14. G. Sedmak, S. Hocevar, J. Levec, Journal of Catalysis 222 (2004) 87.
15. A. Martinez-Arias, A.B. Hungria, G. Munuera, D. Gamarra, Applied Catalysis B 65 (2006) 207.
16. M. Haruta, S. Tsubota, T. Kobayashi, H. Kageyama, M.J. Genet, B. Delmon, Journal of Catalysis 144 (1993) 175.
17. G.C. Bond, D.T. Thompson, Catalysis Reviews 41 (1999) 319.
18. J. Langford, A. Wilson, Journal of Applied Crystallography 11 (1978) 102.
19. D. Andrews, Perspectives in modern chemical spectroscopy, Springer-Verlag, Berlin, 1990.
20. T. Caputo, L. Lisi, R. Pirone, G. Russo, Applied Catalysis A 348 (2008) 42.
21. S. Monyanon, S. Pongstabodee, A. Luengnaruemitchai, Journal of Power Sources 163 (2006) 547.
22. V. Alfredsson, W.M. Anderson, Chemistry of Materials 8 (1996) 1141.
23. X. Liao, W. Chu, X. Dai, V. Pitchon, Applied Catalysis B 142 (2013) 25
24. J.L. Ayastuy, A. Gurbani, M.P. Gonzalez-Marcos, M.A. Gutierrez-Ortiz, International Journal of Hydrogen Energy 35 (2010) 1232.
25. N.K. Gamboa-Rosales, J.L. Ayastuy, M.P. Gonzalez-Marcos, M.A. Gutierrez-Ortiz, International Journal of Hydrogen Energy 37 (2012) 7005.
26. G.W. Graham, W.H. Weber, C.R. Peters, R. Usman, Journal of Catalysis 130 (1991) 310.
27. J.R. McBride, K.C. Haas, B.D. Poindexter, W.H. Weber, Journal of Applied Physics 76 (1994) 2435.
28. O.H. Laguna, M.A. Centeno, M. Boutonnet, J.A. Odriozola, Applied Catalysis B 106 (2011) 621.

29. M. Xiaodong, F. Xi, H. Xuan, G. Hongwen, L. Lu, G. Jie, C. Huiqin, Z. Ting, Microporous and Mesoporous Materials 158 (2012) 214.
30. Z. Zsoldos, F. Gardin, L. Hilaire, L. Guczi, Journal of Molecular Catalysis A 111 (1996) 113.
31. E.B. Fox, S. Velu, M.H. Engelhard, Y.H. Chin, J.T. Miller, J. Kropf, C.S. Song, Journal of Catalysis 260 (2008) 358.
32. Y.C. Wei, C.W. Liu, W.J. Chang, K.W. Wang, Journal of Alloys and Compounds 509 (2011) 535.
33. A. Palermo, F.J. Williams, R.M. Lambert, Journal of Physical Chemistry B 106 (2002) 10215.
34. X. Wang, Q. Kang, D. Li, Catalysis Communications 9 (2008) 2158.
35. R.C. Alvaro, A.D. Ana, M. Elisa, T. Aldo, S. Loretta, L. Maurizio, J.L. Antonio, R.C. Enrique, Journal of Power Sources 196 (2011) 4382.
36. A. Galtayries, R. Sporken, J. Riga, G. Blanchard, R. Caudano, Journal of Electron Spectroscopy and Related Phenomena 88 (1998) 951.
37. J. Avgouropoulos, T. Loannides, Applied Catalysis A 244 (2003) 155.
38. A. Bensalem, F. Bozon-Verduraz, M. Delamar, G. Bugli, Applied Catalysis A 121 (1995) 81.
39. M.I. Zaki, G.A.M. Hussein, S.A.A. Mansour, H.M. Ismail, G.A.H. Mekhemer, Colloids Surface A 127 (1997) 47.
40. H. Praliaud, S. Mikhailenko, Z. Chajar, M. Primet, Applied Catalysis B 16 (1998) 359.
41. Y. Hu, L. Dong, M. Shen, D. Liu, J. Wanf, W. Ding, Applied Catalysis B 31 (2001) 61.
42. R.G. Rango, B.G. Mishra, Bulletin of the Catalysis Society of India 2 (2003) 122.
43. H. Zhu, Z. Qin, W. Shan, W. Shen J. Wang, Journal of Catalysis 225 (2004) 267.
44. J. Xiaoyuan, L. Guanglie, Z. Renxian, M. Jianxin, C. Yu, Z. Xiaoming, Applied Surface Science 173 (2001) 208.
45. G.R. Rao, H.R. Sahu, B.G. Mishra, Colloids and Surfaces A 220 (2003) 261.

46. G. Avgouropoulos, T. Loannides, H. Matralis, Applied Catalysis B 56 (2005) 87.

47. M.F. Luo, Y.J. Zhong, X.X. Yuan, X. Zheng, Applied Catalysis A 162 (1997) 121.

48. A. Martinez-Arias, D. Gamarra, M. Fernandez-Garcia, A. Hornes, P. Bera, Zs. Koppany, Z. Schay, Catalysis Today 143 (2009) 211.

49. D. Gamarra, A. Martinez-Arias, Journal of Catalysis 263 (2009) 189.

50. M. Radovic, Z. Dohcevic-Mitrovic, M. Scepanovic, M. Grujic-Brojcin, B. Matovic, S. Boskovic, Z. V. Popovic, Science of Sintering 39 (2007) 281.

51. E.C.C. Souza, H.F. Brito, E.N.S. Muccillo, Journal of Alloys and Compounds 491 (2010) 460.

52. D.J. Kim, Journal of the American Ceramic Society 72 (1989) 1415.

53. S.J. Hong, A.V. Virkar, Journal of the American Ceramic Society 78 (1995) 433.

54. S.R. Bishop, K.L. Duncan, E.D. Wachsman, Electrochimica Acta 54 (2009) 1436.

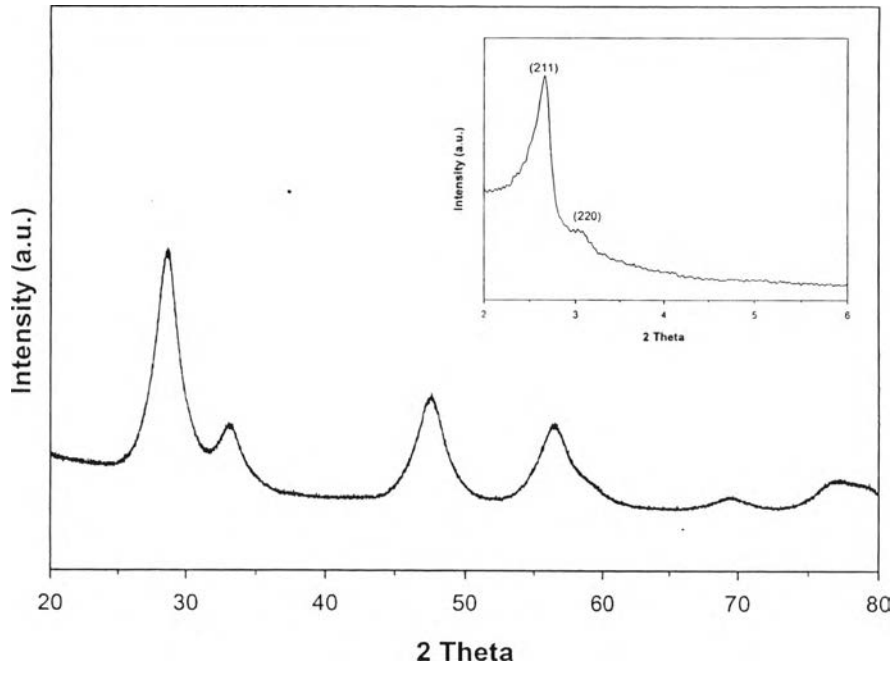

Figure 4.1 WAXD and SAXD (inset) patterns of the synthesized MSP ceria.

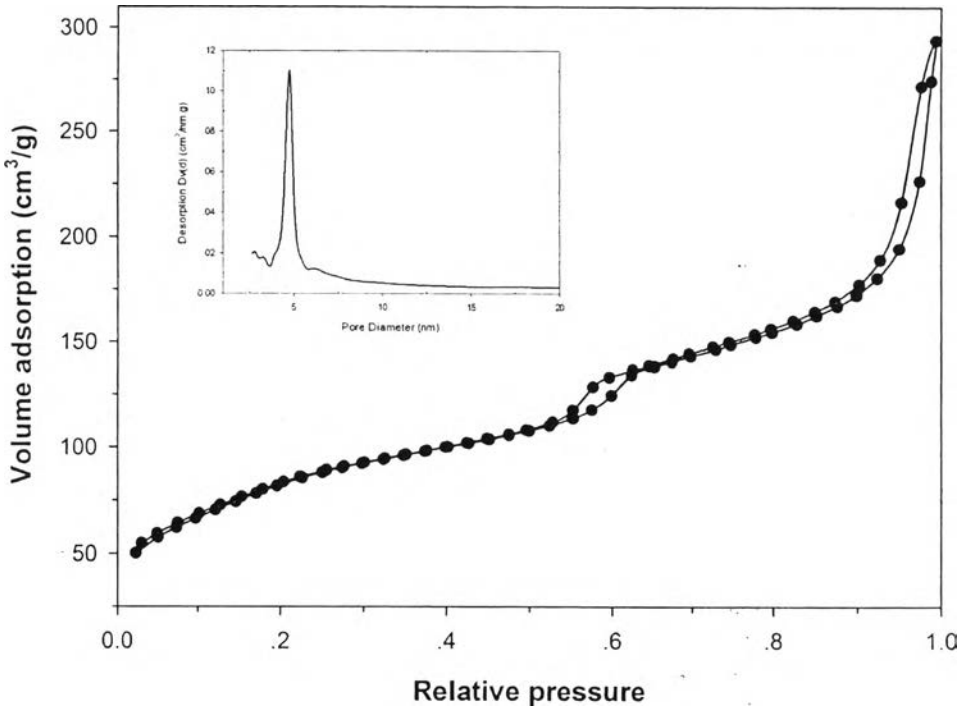

Figure 4.2 N_2 adsorption-desorption isotherms and pore size distribution (inset) of the synthesized MSP ceria.

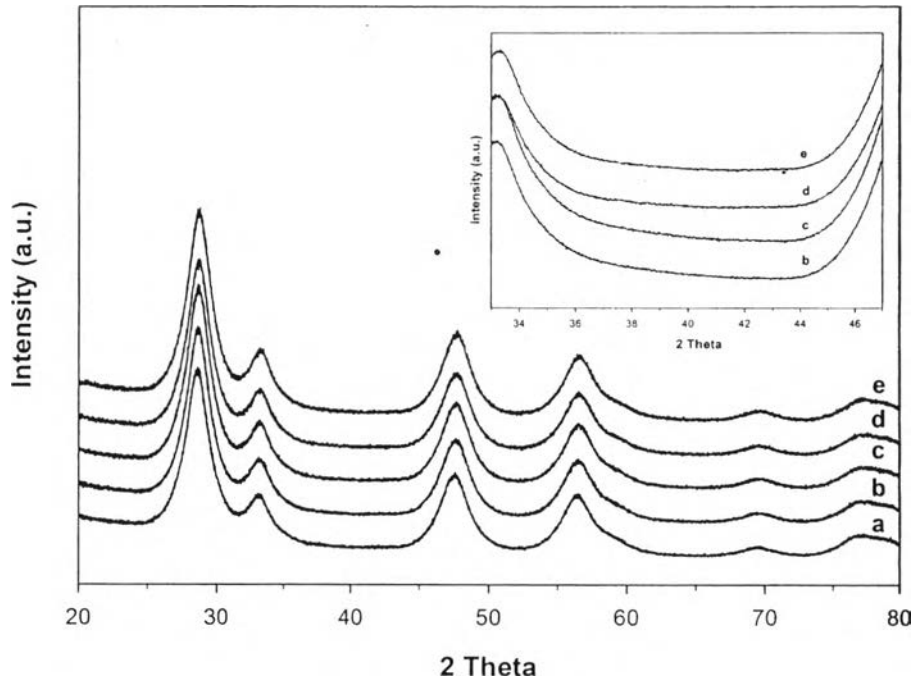

Figure 4.3 XRD patterns with a scanning speed of 1 $^{o}min^{-1}$ and a scanning speed of 0.01$^{o}min^{-1}$ (inset) of (a) pure MSP ceria, (b) $3CuO/CeO_2$, (c) $5CuO/CeO_2$, (d) $7CuO/CeO_2$, and (e) $9CuO/CeO_2$.

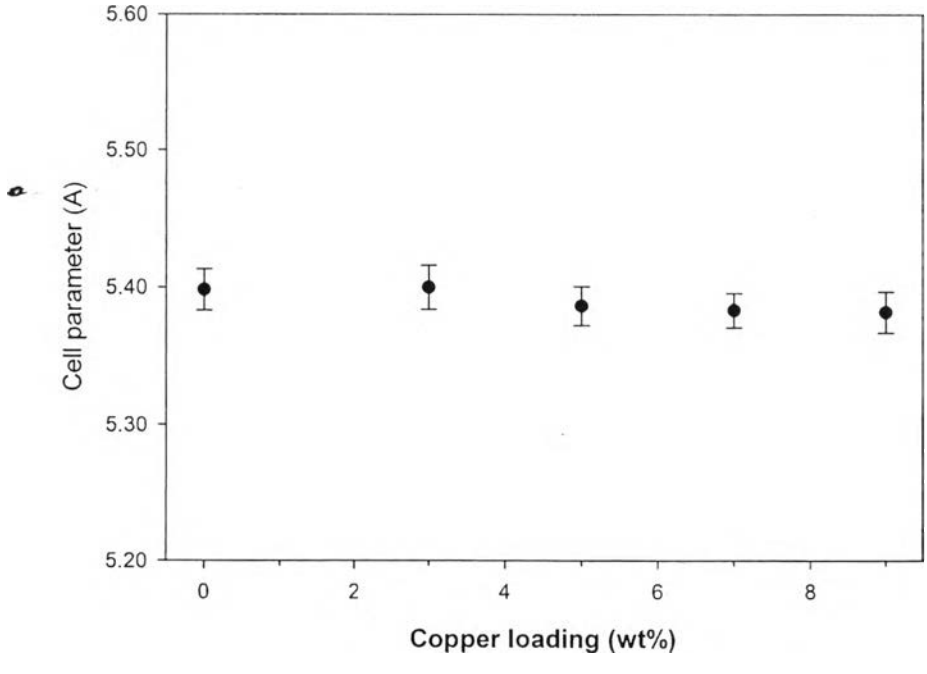

Figure 4.4 Lattice parameters determined by XRD for MSP ceria loaded with different Cu content.

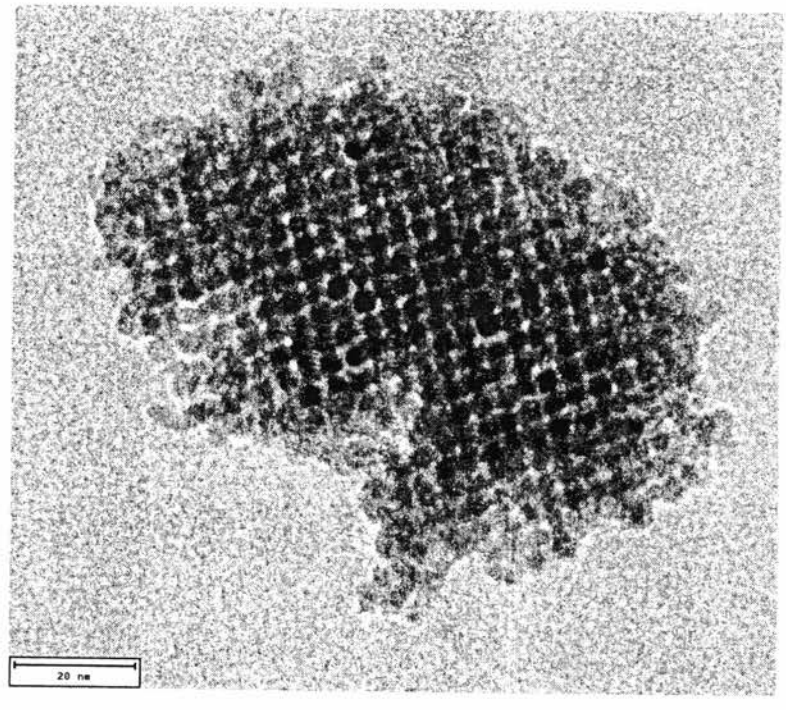

Figure 4.5 TEM image of 7Cu/MSP ceria calcined at 500 °C.

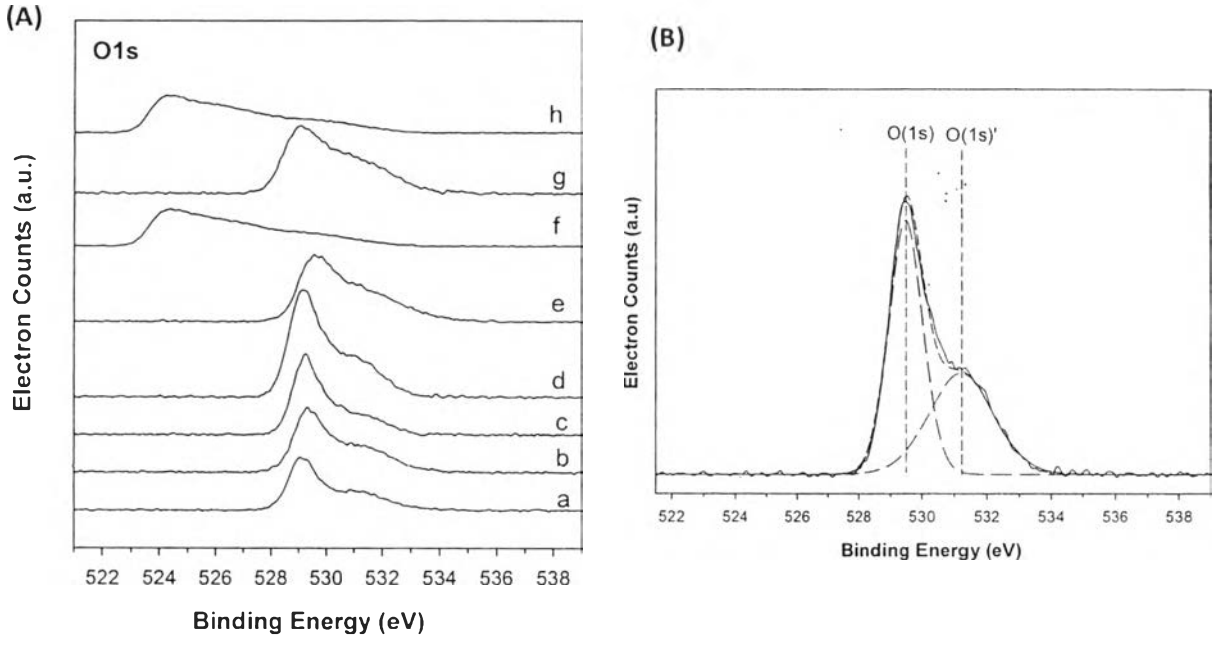

Figure 4.6 (A) O1s XPS spectra of fresh and used (-P) catalysts (a) pure MSP ceria, (b) 3CuO/CeO_2, (c) 5CuO/CeO_2, (d) 7CuO/CeO_2, (e) 9CuO/CeO_2, (f) 7CuO/CeO_2-P1, (g) 7CuO/CeO_2-P2, (h) 7CuO/CeO_2-P3; (B) Example of deconvolution of O1s spectrum of 7CuO/CeO_2.

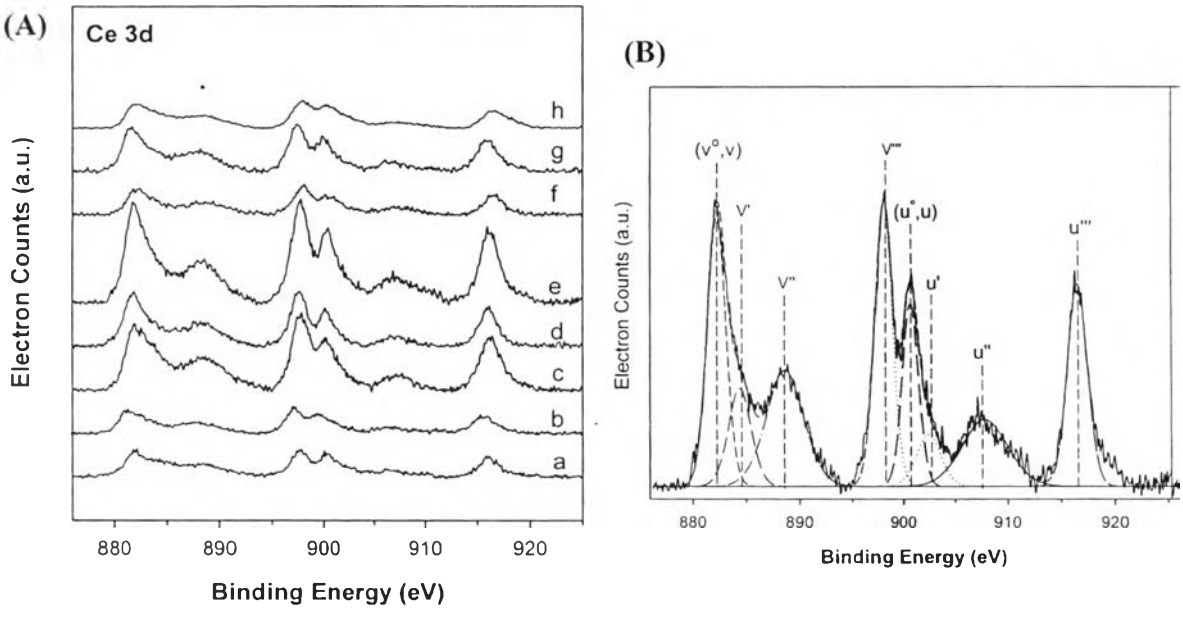

Figure 4.7 (A) Ce3d XPS spectra of fresh and used (-P) catalysts (a) pure MSP ceria, (b) $3CuO/CeO_2$, (c) $5CuO/CeO_2$, (d) $7CuO/CeO_2$, (e) $9CuO/CeO_2$, (f) $7CuO/CeO_2$-P1, (g) $7CuO/CeO_2$-P2, (h) $7CuO/CeO_2$-P3; (B) Example of deconvolution of Ce3d spectra of $7CuO/CeO_2$.

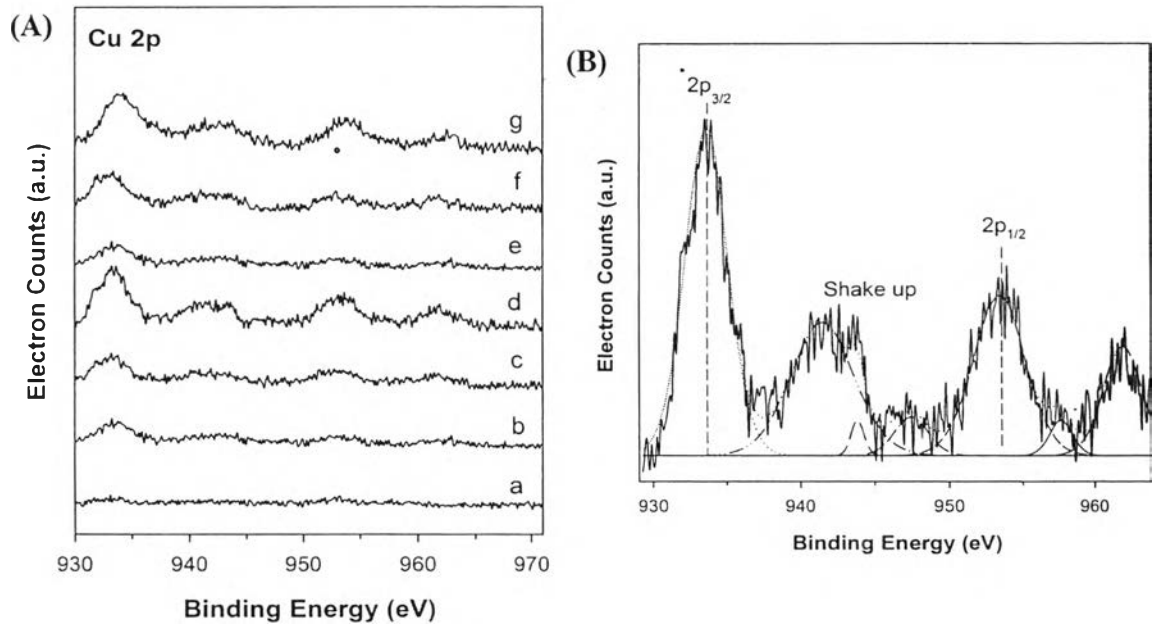

Figure 4.8 (A) Cu 2p XPS spectra of fresh and used (-P) catalysts (a) pure MSP ceria, (b) $3CuO/CeO_2$, (c) $5CuO/CeO_2$, (d) $7CuO/CeO_2$, (e) $9CuO/CeO_2$, (f) $7CuO/CeO_2$-P1, (g) $7CuO/CeO_2$-P2, (h) $7CuO/CeO_2$-P3; (B) Example of deconvolution of Cu2p spectra of $9CuO/CeO_2$.

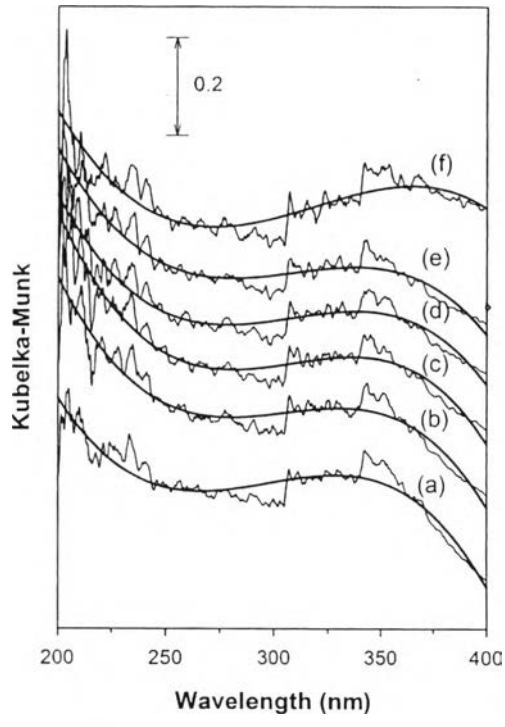

Figure 4.9 Kubelka-Munk function from UV-Vis DRS spectra of (a) pure MSP ceria, (b) $3CuO/CeO_2$, (c) $5CuO/CeO_2$, (d) $7CuO/CeO_2$, (e) $9CuO/CeO_2$, (f) Pure CuO.

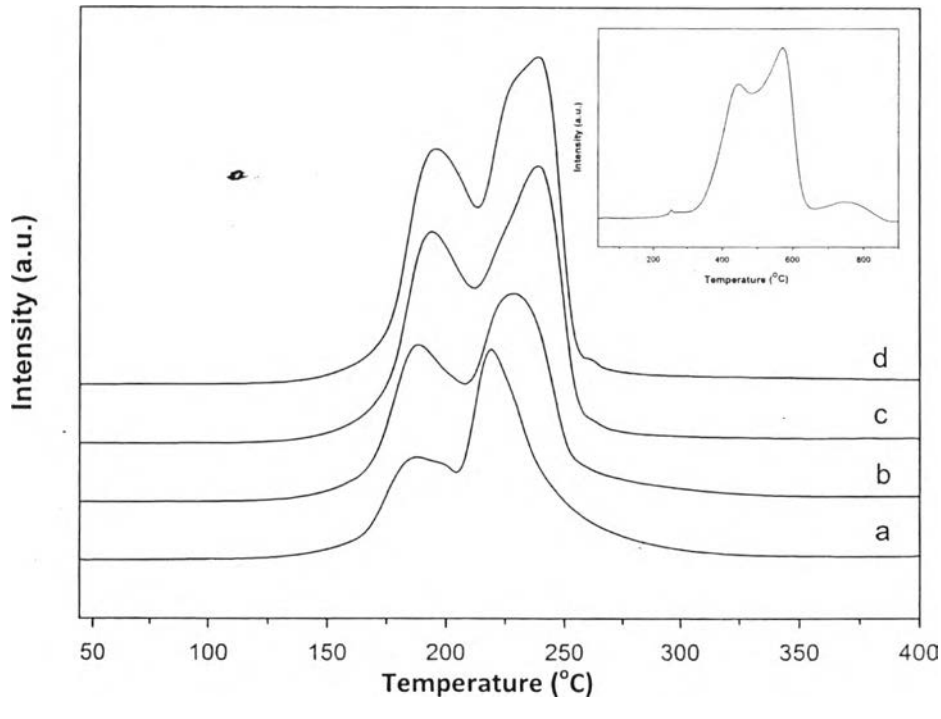

Figure 4.10 H_2-TPR profiles of (a) $3CuO/CeO_2$, (b) $5CuO/CeO_2$, (c) $7CuO/CeO_2$, (d) $9CuO/CeO_2$ and pure MSP ceria (inset).

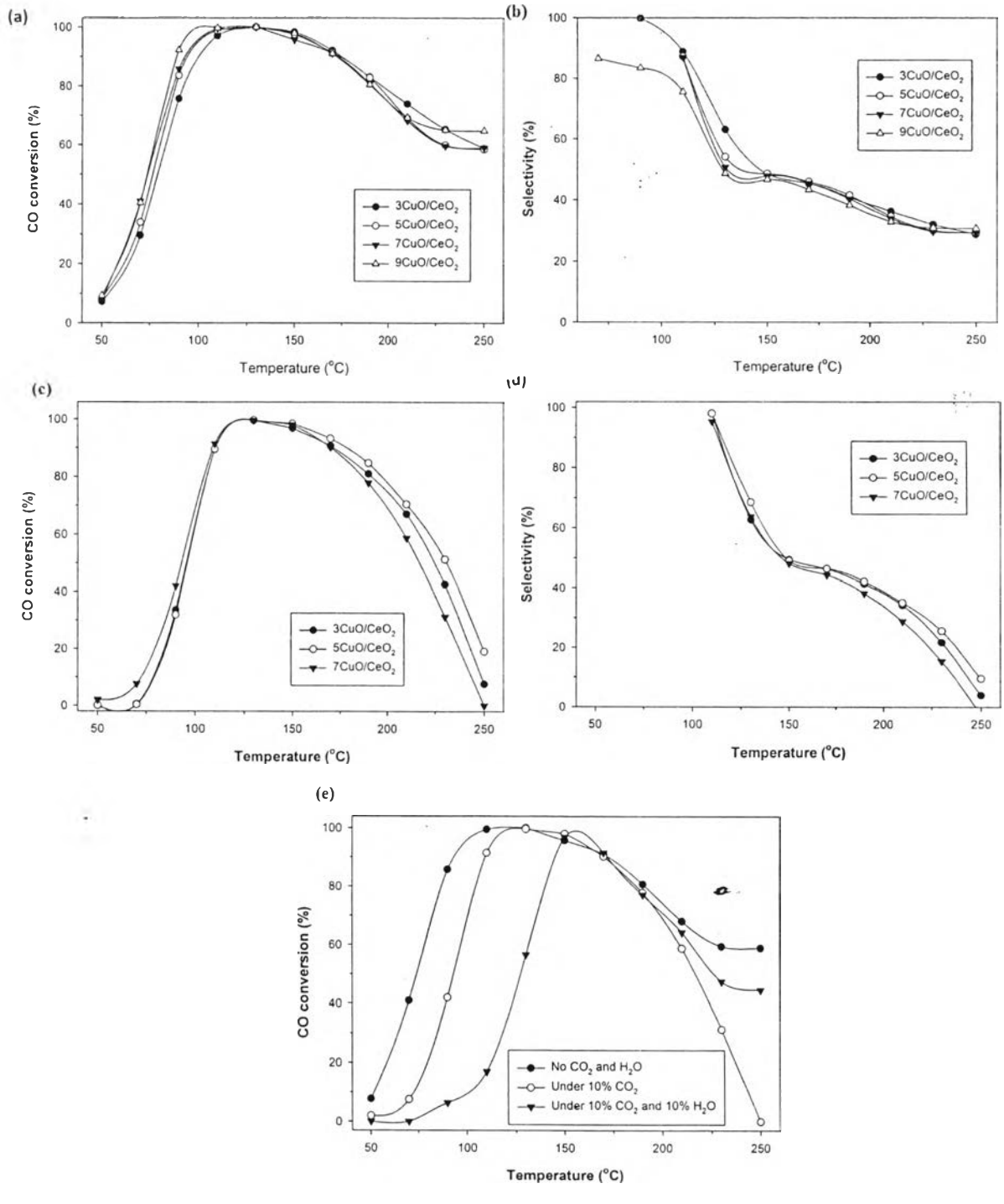

Figure 4.11 (a) CO conversion and (b) selectivity for PROX reaction using feed composition of 1%CO, 1%O_2, 40%H_2 balance in He (c) CO conversion and (d) selectivity for PROX reaction in the present of 10 % CO_2 (e) CO conversion of 7CuO/CeO_2 for PROX reaction in various feed compositions.

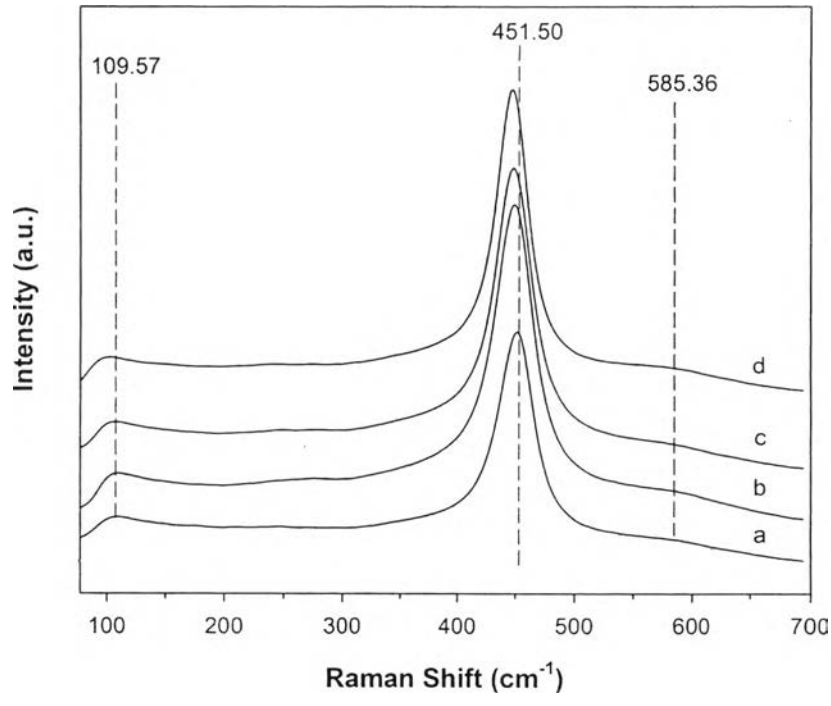

Figure 4.12 Raman spectra of fresh and used (-P) catalysts after stability test for PROX reaction (a) fresh 7CuO/CeO_2, (b) 7CuO/CeO_2-P1, (c) 7CuO/CeO_2-P2, (d) 7CuO/CeO_2-P3.

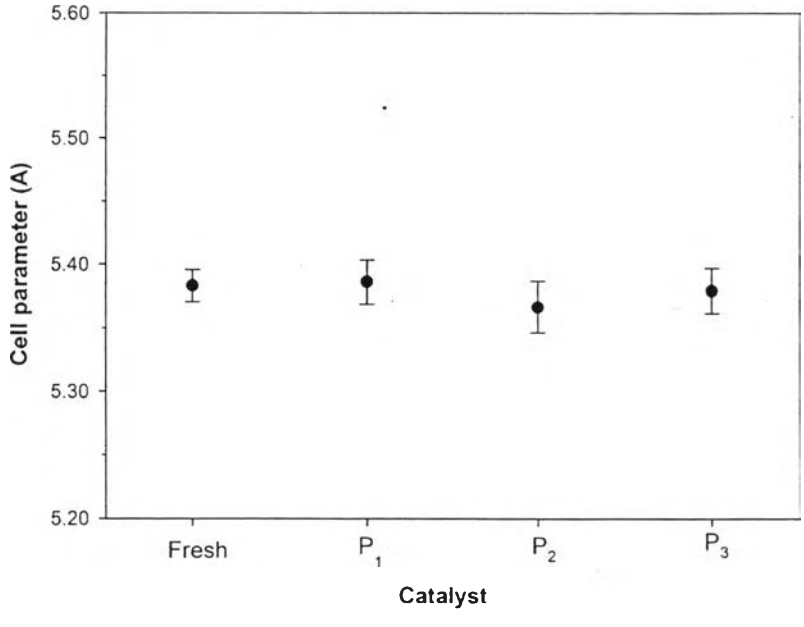

Figure 4.13 Lattice parameters determined by XRD for fresh and used catalysts after stability test for PROX reaction.

Table 4.1 Properties of MSP CeO_2 and CuO/CeO_2 catalyst

Catalyst	Cu(%)[t]	Cu(%)[a]	S_{BET} (m^2/g)	Average size of ceria particles (nm)	Lattice parameter (Å)
MSP CeO_2	-	-	293.2	3.75	5.39
$3CuO/CeO_2$	3.00	2.90	257.4	3.82	5.39
$5CuO/CeO_2$	5.00	4.96	240.3	3.81	5.38
$7CuO/CeO_2$	7.00	6.95	229.5	3.84	5.38
$9CuO/CeO_2$	9.00	9.10	201.7	3.82	5.38

[t] Theoretical value

[a] from AAS

Table 4.2 Relationship of species distribution on the surface of catalysts by XPS

Catalyst	Cu on surface	$O_{lattice}/(O_{OH}+O_{abs})$	$I_{Cu,sat}/I_{Cu2p3/2}$	Position of shake up (Cu-2p)	Ce^{3+} $3d_{5/2}$ (%)
MSP CeO_2	-	1.51	-	-	37.8
$3CuO/CeO_2$	1.31	0.99	0.51	941.52	38.7
$5CuO/CeO_2$	2.28	1.14	0.50	941.57	38.6
$7CuO/CeO_2$	4.34	1.30	0.49	941.92	37.7
$9CuO/CeO_2$	5.87	1.25	0.50	942.02	36.7
$7CuO/CeO_2$-P1	-	0.28	0.48	941.88	37.8
$7CuO/CeO_2$-P2	-	0.51	0.46	941.72	40.1
$7CuO/CeO_2$-P3	-	0.34	0.47	941.926	39.4

Table 4.3 H_2-TPR results of all catalysts

Catalyst	H_2 uptake of 1^o peak	H_2 uptake of 2^o peak	Theoretical H_2 uptake ($\mu molg^{-1}$) Cu^{2+} to Cu^0	H_2 uptake of MSP CeO_2 ($\mu molg^{-1}$) Ce^{4+} to Ce^{3+}
$3CuO/CeO_2$	450.0	1134.1	487	647.1
$5CuO/CeO_2$	673.0	1201.6	828	373.6
$7CuO/CeO_2$	948.4	1314.4	1184	130.4
$9CuO/CeO_2$	1047.6	1588.5	1556	32.5